Evaluation of Extratropical Cyclone Precipitation in the North Atlantic Basin: An Analysis of ERA-Interim, WRF, and Two CMIP5 Models

JAMES F. BOOTH

City College of the City University of New York, and NASA Goddard Institute for Space Studies, New York, New York

CATHERINE M. NAUD

Columbia University, and NASA Goddard Institute for Space Studies, New York, New York

JEFF WILLISON

North Carolina State University, Raleigh, North Carolina

(Manuscript received 12 May 2017, in final form 13 December 2017)

ABSTRACT

The representation of extratropical cyclone (ETC) precipitation in general circulation models (GCMs) and the Weather Research and Forecasting (WRF) Model is analyzed. This work considers the link between ETC precipitation and dynamical strength and tests if parameterized convection affects this link for ETCs in the North Atlantic basin. Lagrangian cyclone tracks of ETCs in ERA-Interim (ERAI), GISS and GFDL CMIP5 models, and WRF with two horizontal resolutions are utilized in a compositing analysis. The 20-km-resolution WRF Model generates stronger ETCs based on surface wind speed and cyclone precipitation. The GCMs and ERAI generate similar composite means and distributions for cyclone precipitation rates, but GCMs generate weaker cyclone surface winds than ERAI. The amount of cyclone precipitation generated by the convection scheme differs significantly across the datasets, with the GISS model generating the most, followed by ERAI and then the GFDL model. The models and reanalysis generate relatively more parameterized convective precipitation when the total cyclone-averaged precipitation is smaller. This is partially due to the contribution of parameterized convective precipitation occurring more often late in the ETC's life cycle. For reanalysis and models, precipitation increases with both cyclone moisture and surface wind speed, and this is true if the contribution from the parameterized convection scheme is larger or not. This work shows that these different models generate similar total ETC precipitation despite large differences in the parameterized convection, and these differences do not cause unexpected behavior in ETC precipitation sensitivity to cyclone moisture or surface wind speed.

1. Introduction

Extratropical cyclones (ETCs) are responsible for the majority of wintertime precipitation in the midlatitudes (e.g., Hawcroft et al. 2012). For general circulation model (GCM) projections of this midlatitude precipitation to be useful, the models should accurately capture ETC precipitation in the current climate. One process that may be a particular issue for GCMs is latent heating within the cyclones (Willison et al. 2015; Hawcroft et al. 2017), which is related to cyclone precipitation and can affect the dynamical strength of the cyclone (e.g., Emanuel et al. 1987; Stoelinga 1996), and this change in dynamics can feedback on the precipitation amount. Recent work suggests that parameterized convection in models can impact the moisture content within a cyclone's warm conveyor belt (WCB; e.g., Carlson 1998, p. 305) by transporting the moisture upward and out of the WCB at the WCB entrance region (Boutle et al. 2011; Booth et al. 2013). Following this chain of reasoning, the present study examines ETC precipitation and the precipitation generated by the

Denotes content that is immediately available upon publication as open access.

Corresponding author: James F. Booth, jbooth@ccny.cuny.edu

DOI: 10.1175/JCLI-D-17-0308.1

convection scheme in a reanalysis, GCMs, and a regional climate model. The research is focused on determining the skill of the reanalysis and the different models, relative to each other, in generating ETC precipitation and determining if the contribution of precipitation from the convection scheme impacts the relationship between the cyclones and their water vapor content and surface winds.

The analysis will utilize cyclone-centered compositing, which is a useful tool for bulk comparisons of ETCs across datasets that do not have identical ETC tracks. Previous work has shown that GCMs with horizontal resolution of less than 1° are capable of generating realistic winds and precipitation composites (Field et al. 2008; Bengtsson et al. 2009; Catto et al. 2010; Hawcroft et al. 2016). The Bengtsson et al. (2009) study also found that a model with approximately 2° resolution did not produce strong enough ETCs in terms of both winds and precipitation. The present work seeks to extend those previous analyses by considering two models with 2° × 2.5° resolution: the Geophysical Fluid Dynamics Laboratory (GFDL) model and the NASA Goddard Institute for Space Studies (GISS) model from phase 5 of the Coupled Intercomparison Project (CMIP5). This analysis is part of a project in collaboration with the modeling centers focused on testing and improving moist processes in their GCMs. Of particular interest is the impact of parameterizations on ETCs; here, we will focus on parameterized convection.

In both the GFDL and the GISS GCMs, there is a single convection parameterization used globally, meaning the schemes in the models are usually designed with attention on the tropics. In contrast, the Weather Research and Forecasting (WRF) Model (Skamarock et al. 2008) was developed originally for forecasting midlatitude weather. These different constraints on parameterized physics motivate us to compare ETC precipitation between GCMs and WRF. Herein, we analyze ETC precipitation from integrations in which WRF was configured as a regional climate model (Willison et al. 2015; Michaelis et al. 2017).

As part of the comparison of the datasets, we will test model ETC precipitation sensitivity to changes in cyclone moisture and wind speed. This is motivated by the WCB rain model of Field and Wood (2007; hereinafter FW2007). Given the observational data available, FW2007 developed the following model:

$$R_{\mathrm{WCB}} = k \times \mathrm{PWV} \times \mathrm{WSPD} \qquad (1).$$

In (1), PWV and WSPD are cyclone-averaged values of precipitable water vapor and surface wind speed, respectively. This model has been used for analyzing GCM precipitation (Field et al. 2008) and determining that changes in ETC precipitation are predominantly caused by changes in PWV, not WSPD in a GCM projection of global warming (Yettella and Kay 2017). The fit of the R_{WCB} model can vary with cyclone life cycle and latitude (Pfahl and Sprenger 2016), and this will be considered in our analysis.

As mentioned above, there is reason to ask if parameterized convection impacts the relationship between ETC precipitation and surface wind speed. Boutle et al. (2011) and Booth et al. (2013) show that if parameterized convection is active in the equatorward region of a modeled ETC's warm sector, it can remove moisture from the WCB. In addition, the different vertical distribution of heating profiles typically associated with convection and isentropic ascent can impact cyclone development (Tierney et al. 2017, manuscript submitted to *Climate Dyn.*). Therefore, the analysis herein uses cyclone-centered compositing to analyze the relationships among dynamical strength, precipitation, and parameterized convection within ETCs. However, in the feedback loop between precipitation and surface wind speed, we will only focus on one direction: the response of precipitation to changes in wind speed.

The results section of the paper is organized as follows. First, we analyze the distribution of ETC strength, which is motivated by the fact that latent heating associated with precipitation can impact cyclone strength. This is followed by analyses of the composite means and distributions of ETC precipitation rates, as well as the precipitation generated by the convection scheme. We find that total precipitation is similar for most of the datasets, despite large differences in precipitation amount generated by the convection scheme. Therefore, we characterize the behavior of convective precipitation across the different datasets. Finally, we examine the sensitivity of modeled ETC precipitation to changes in cyclone water vapor and surface wind speed, including whether the sensitivity is affected by precipitation from the convection scheme. This work provides information on both the behavior of parameterized convective precipitation in ETCs and its potential impact on the ETC precipitation, and to our knowledge, it is the first direct comparison of ETC precipitation between the GCMs and WRF.

2. Data and methods

Table 1 provides a summary of the datasets used in this analysis. The WRF data were produced for a limited regional domain and a specific season and time period. Therefore, the same domains and time periods are used for reanalysis and GCM output when possible.

TABLE 1. Details for models and track and cyclone counts. (Expansions of acronyms are available online at http://www.ametsoc.org/PubsAcronymList.)

Reanalysis and model overview				
	Atmosphere resolution (lat × lon)	Convection scheme	Track count	Cyclone count
ERA-Interim (Dee et al. 2011)	0.7° × 0.7° (spectral T255)	Tiedtke (1989)	353	4446
GFDL CM3 (Donner et al. 2011)	2° × 2.5°	Donner (1993)	310	4210
GISS-E2-H (Schmidt et al. 2014)	2° × 2.5°	Yao and Del Genio (1989) and Kim et al. (2011)	282	4093
WRF RCM (Willison et al. 2015)	120 km × 120 km	Zhang and McFarlane (1995)	224	2836
	20 km × 20 km		266	3057

Two configurations of a WRF regional climate model (RCM) are used, both of which have been described in detail in Willison et al. (2015). One configuration has a horizontal resolution of 120 km (hereinafter WRF-120km). The second version has a horizontal resolution of 20 km (hereinafter WRF-20km). These resolutions were chosen because they are typical resolutions of GCMs (i.e., the 120-km model) and regional climate models (20 km). The WRF domain covers the North Atlantic Ocean, extending from 15° to 72°N and from 96°W to 46°E. The model lateral boundary conditions and surface conditions are from the NCEP final analyses (NCEP/NWS/NOAA/U.S. Department of Commerce 2000). Starting in 2001 and ending in 2010, model runs begin on 24 December and continue until 7 April of the following year. The first week of each winter's integration is not used in order to avoid issues with model spinup, so the analysis focuses on January–March (JFM) for 2002–11. See Willison et al. (2015) for a discussion of model setup, spinup, and sensitivities.

The reanalysis used is ERA-Interim (ERAI; Dee et al. 2011). The time period used is 2002–11, and the months used are January–March. ERAI has been shown to compare well with other reanalysis data for ETC dynamical strength and spatial distribution (Hodges et al. 2011). Based on daily means, ERAI precipitation compared reasonably well (Hawcroft et al. 2012) with the Global Precipitation Climatology Project dataset (Adler et al. 2003). Based on recent analysis of ETC precipitation composites based on instantaneous satellite data, it appears that ERAI might slightly underestimate ETC precipitation; however, the ERAI bias is no larger than differences among multiple satellite platforms (Naud et al. 2017, manuscript submitted to *J. Appl. Meteor. Climatol.*).

As mentioned in section 1, the GCMs used for this study are GFDL CM3 and GISS ModelE2. For GFDL CM3 (Donner et al. 2011), we use the first member configuration (i.e., r1i1p1) from the historical CMIP5 experiment. The data were downloaded from the GFDL National Operational Model Archive and Distribution System (NOMADS) portal. This model's integration ended in 2005; therefore, data from January to March for the years 1996–2005 are used in the analysis. For the NASA GCM, we use the GISS ModelE2 (Schmidt et al. 2014). As with the GFDL model, we use the r1i1p1 version of the model. GISS submitted two versions of the model to the CMIP5 catalog; here, we analyze the model version using the Hybrid Coordinate Ocean Model (HYCOM; Bleck 2002), referred to as GISS-E2-H in CMIP5. To match the GFDL model, data from January to March for 1996–2005 are used. These models will be referred to as GFDL and GISS, respectively.

Before doing any cyclone-tracking, statistics, or compositing analysis, the reanalysis and WRF RCM data are regridded to the 2° × 2.5° horizontal resolution grid used by the GCMs. The regridding is accomplished using the Computational Information Systems Laboratory (CISL)'s NCAR Command Language (NCL) tools. This method uses an inverse-distance-squared weighting of the four points in the WRF grid that are closest to each point in the GCM grid. Although this scheme makes an "area mean" assumption, it is nonconservative. This can lead to the possibility of more extreme values (Chen and Knutson 2008). However, we ran comparisons of the precipitation distributions for the original and regridded data and found that the impact of regridding on the largest precipitation rates are less than 1% for the distributions we analyze. For the regridded data, there is a 4% increase in the occurrence of smaller precipitation rates (i.e., the 0–1 mm day^{-1} range) and a corresponding decrease in the occurrence of zero precipitation. However, the overall shapes of the distributions do not change before and after regridding. Given the availability and portability of NCL, we chose to use its regridding scheme because it allows for easy reproducibility of the analysis.

The variables analyzed here are precipitation, convective precipitation, sea level pressure (SLP), specific humidity at 850 hPa (Q850), and 10-m wind speed. For precipitation, WRF and ERAI provide accumulated data every 6 h. In the case of ERAI, we do not use the

data generated during the first 6 h of the forecast (referred to here as the reanalysis version), as it has been found to have a spinup bias (Hawcroft et al. 2016). By using the forecast product for precipitation and reanalysis version for the cyclone locations for ERAI, we may introduce small differences in the location of the cyclone center relative to the precipitation. We bear this in mind for the interpretation of the results. The GFDL model provides 3-hourly time-averaged precipitation that we average into 6-hourly data. The GISS model provides 6-hourly time-averaged data. We multiply the 6-hourly data by 4 to obtain units of millimeters per day, for consistency with FW2007.

For our analysis of the WCB rain model, we use Q850, not PWV (as in FW2007), because the CMIP5 data archive does not include 6-hourly PWV data. We use ERAI to test if this replacement is reasonable. For the Northern Hemisphere, for the latitudes between 20° and 65°N, we calculate the spatial correlation of 6-hourly snapshots of PWV and Q850 for a set of 100 randomly selected dates. For these cases, the correlation between PWV and Q850 has an average value of 0.92 and is never less than 0.9. If the land is excluded, the average correlation value is 0.94. We also create a linear estimate of PWV from Q850 and find that large biases rarely occur and do not systematically affect specific cyclone regions. Therefore, given the availability of data, the analysis reported here will use Q850 in the WCB model.

Extratropical cyclone tracks in the models and reanalysis are identified using the Lagrangian tracking algorithm of Bauer et al. (2016), which is an update of the algorithm in Bauer and Del Genio (2006). The algorithm identifies low pressure centers, using 6-hourly SLP fields, and then the cyclones are linked into tracks. Bauer et al. (2016) show that the skill of their algorithm compares well with multiple other tracking programs summarized in Neu et al. (2013). The term cyclone refers to 6-hourly snapshots, and track refers to the full life cycle.

For the GCM and reanalysis, the tracking algorithm can be applied to global data, whereas the RCM only has data for its specified domain. Therefore, a set of criteria is used to homogenize the GCM and ERAI tracks in order to minimize biases associated with the RCM's limited domain. To account for the fact that the RCM might have biases in track genesis near its edges, we remove any tracks in which all of the cyclone centers are (i) north of 55°N, (ii) south of 36°N, (iii) west of 72°W, or (iv) east of 5°E. Also, any individual cyclones outside of the RCM domain are removed (the remainder of the track is retained). Then, we check that the portion of the track that remains would have been retained by the Bauer et al. (2016) tracker, based on its duration and propagation distance (otherwise, the equivalent tracks would not be in the RCM track data). Any tracks with total travel distances less than 500 km are presumed to be cutoff lows associated with topography and are removed (see Bauer et al. 2016).

Our preliminary analysis identified a large difference in WSPD for cyclones over land in both WRF Model configurations compared to the reanalysis and GCMs. This may be due to differences in the models' surface layer schemes. Therefore, we masked land points and only analyzed cyclones for which at least 50% of the region within 1000 km of the center is over ocean (ocean cyclones). To accomplish this, we test each track for ocean cyclones and remove those that are not. Then, we test if the track still has at least five cyclones adjacent in time. If so, we retain the new track consisting only of the ocean cyclones that are adjacent in time. These tracks are used for the remainder of the analysis and are summarized in Table 1.

Figure 1a shows cyclone density for ERAI. Note that the region shown is smaller than the WRF domain. The maximum near the Gulf Stream region and the southwest–northeast tilt in the cyclone density exists for all of the models (not shown). The reanalysis and GCMs have 5%–15% more tracks on the western half of the ocean basin than the WRF Model configurations. To test if this affects the results, we randomly subsampled the tracks from all of the models to have a matching number of 200. The results using this subset are very similar to the results using the full set of cyclones; therefore, we report the results using all cyclones. Figure 1b shows that the models and reanalysis have similarly distributed cyclones with respect to latitude; however, the maxima for the GCMs are south of those from the reanalysis. This issue with GCMs could be related to cyclone steering [for details on steering see Booth et al. (2017)], and the steering biases may be associated with model representation of orographic drag (Pithan et al. 2016). To account for the differences in latitudinal distribution of the cyclones, we randomly subsampled cyclones per 4° latitude bin so that each dataset had the same number of cyclones per bin and repeated our analysis. This also did not have a noticeable impact; therefore, we use the cyclones shown in Fig. 1b.

To calculate cyclone-centered averages, we identify all data within 1000 km of each cyclone's center, using the 2° × 2.5° regridded data. For cyclone-centered averaging, we calculate area-weighted averages of the data on the geographic grid. The distance of 1000 km differs from FW2007, who use 2000 km. The choice of a smaller radius is motivated by the fact that latent heating close to the cyclone center (where potential vorticity tends to be stronger) can have a larger impact on the dynamics (e.g., Martin 2006, p. 293). As discussed above, we mask out

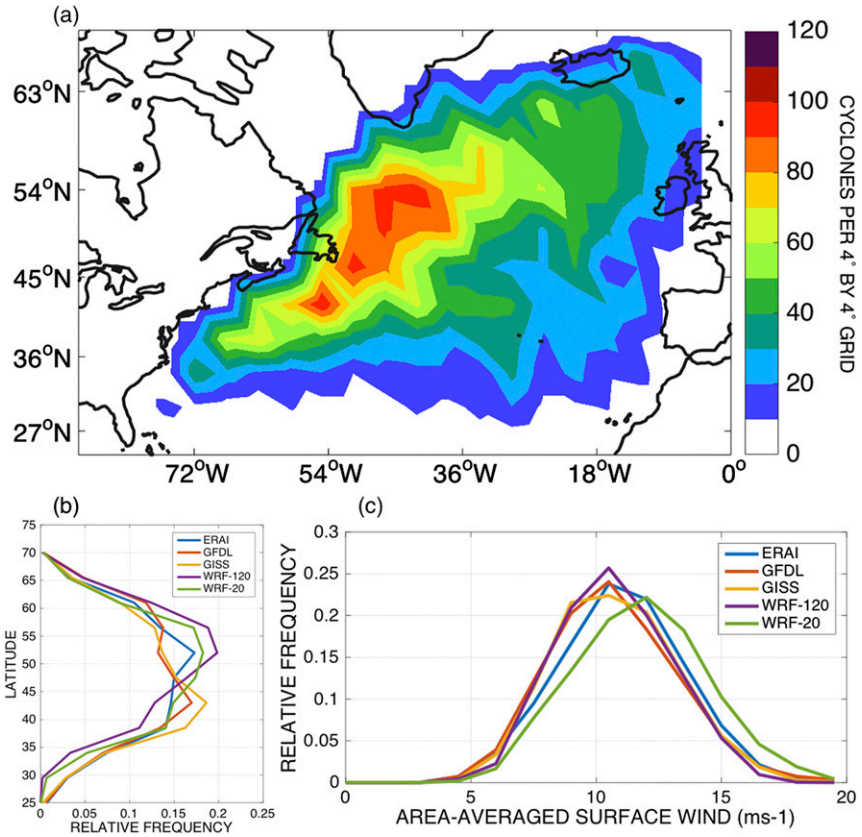

FIG. 1. (a) Cyclone density per 4° × 4° grid box for ERAI, (b) latitudinal distribution of cyclones per model, and (c) distribution of cyclone-averaged surface wind speed.

areas over land. For composite figures, we show results extending out to 2000 km, for ease of comparison with FW2007. We project cyclone-centered data to a stereographic projection, taking into account the different distances from the cyclone center for different latitudes. For the composites, we do not rotate the fields relative to the cyclone propagation direction, as we found that it had only minimal impact on the results. We note that small differences in the location of the peak precipitation relative to the cyclone center will not be a focus of this study, as they might relate to issues of using ERAI forecast products for precipitation but not for SLP.

Significance tests for the distributions are conducted using the Kolmogorov–Smirnov goodness-of-fit test at a 99% significance interval. This tests the null hypothesis that two distributions are drawn from the same population. Therefore, in cases in which we consider multiple distributions, we compare each pair individually.

3. Results

The analysis is separated into three sections. First, cyclone dynamical strength and precipitation strength are examined, both to compare the models with reanalysis and to provide a bulk analysis of the relationship between latent heating associated with cyclone precipitation and cyclone circulation strength. Then, motivated by the potential impact of convection on ETC latent heating, the role of precipitation from convective parameterizations is analyzed. Finally, ideas from the first two sections are brought together in an analysis of the sensitivity of total precipitation to cyclone surface wind speed and moisture for subsets with different levels of convective activity.

a. Cyclone dynamical strength and precipitation

As discussed above, in-cyclone latent heating, which is associated with the cyclone's precipitation, can strengthen the cyclones dynamically. Therefore, we begin with an analysis of cyclone dynamical strength based on WSPD. We choose WSPD because it relates to storm damage (e.g., Shimkus et al. 2017; Walz et al. 2017, and references therein) and 850-hPa relative vorticity, which is a common metric in cyclone-tracking studies (e.g., Zappa et al. 2013). The WRF-20km model has the highest frequency of strong cyclones, followed by ERAI (Fig. 1c). WSPD

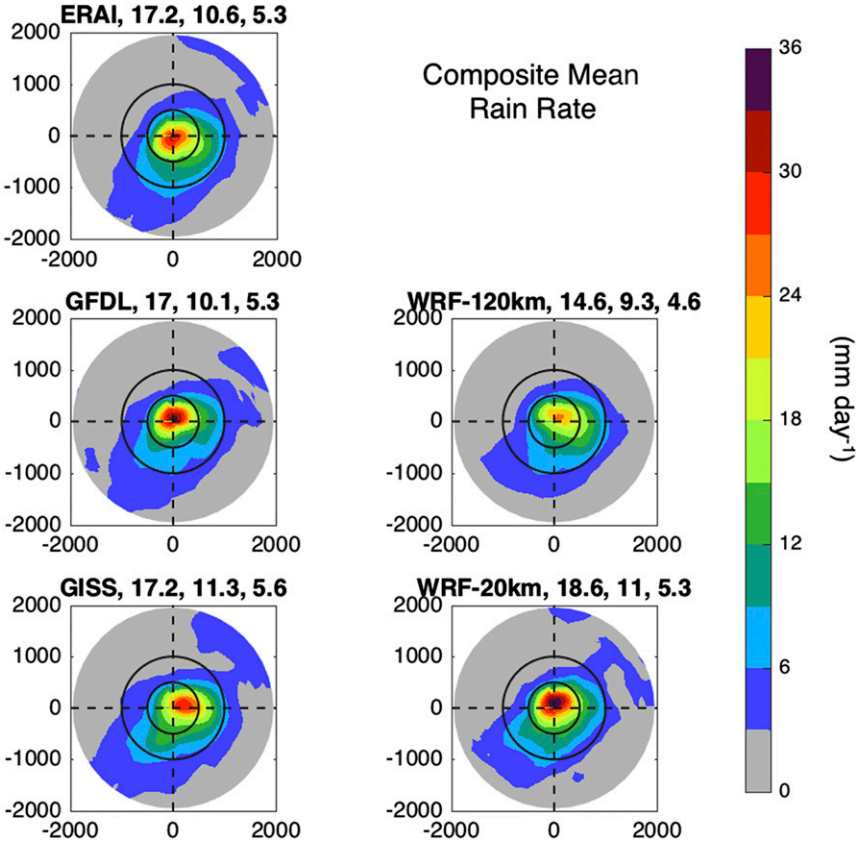

FIG. 2. Cyclone-centered composite mean precipitation. Cyclones used in each composite at the time of cyclone-averaged precipitation maximum per track. Black circles indicate 500- (inner) and 1000-km (outer) radii. Values given above each panel are the cyclone-averaged precipitation (mm day^{-1}) for 500, 1000, and 2000 km.

distribution from WRF-20km is shifted toward stronger values relative to those of the other models, based on the Kolmogorov–Smirnov goodness-of-fit test. Using the same test, cyclones in ERAI also tend to be stronger than those in the GFDL, GISS, and WRF-120km models. These model-to-model differences in WSPD can have big impacts because storm damage relates to the cube of wind speed (e.g., Leckebusch et al. 2008). An analysis of the distributions of cyclone central SLP also reveals that ERAI and WRF-20km have deeper cyclones more frequently than the other models (not shown). Both the WSPD and SLP results look similar when we subsample the datasets to account for the differences in their latitudinal distributions; therefore, they are not shown.

Next, we consider cyclone-centered precipitation composites using cyclones that have the strongest cyclone-averaged precipitation rate per cyclone track. We focus on this snapshot in the life cycles because of the two-way link between precipitation and dynamical strength, which we do not want to lose by averaging the different precipitation patterns that emerge throughout the life cycle (Rudeva and Gulev 2011). Figure 2 shows that the reanalysis and models all generate a similar spatial pattern: a comma shape with a maximum near the cyclone center extending slightly east. The southwestward extension of precipitation from the cyclone center indicates the location of the cold fronts. Cyclone average values at 500, 1000, and 2000 km are included in Fig. 2 to help quantify model-to-model similarities and differences. ERAI and the GFDL, GISS, and WRF-20km models have good agreement in magnitude (the differences are less than 10% based on 500-km cyclone average), but there are some differences. GFDL generates more precipitation than ERAI toward the cyclone center and less in the cold-frontal region within 1000 km of the center. In contrast, the GISS model matches ERAI near the center but generates more precipitation than ERAI in the cold front region. The WRF-120km model has too little precipitation everywhere. The WRF-20km model generates the most precipitation. Bengtsson et al. (2009) also found that their

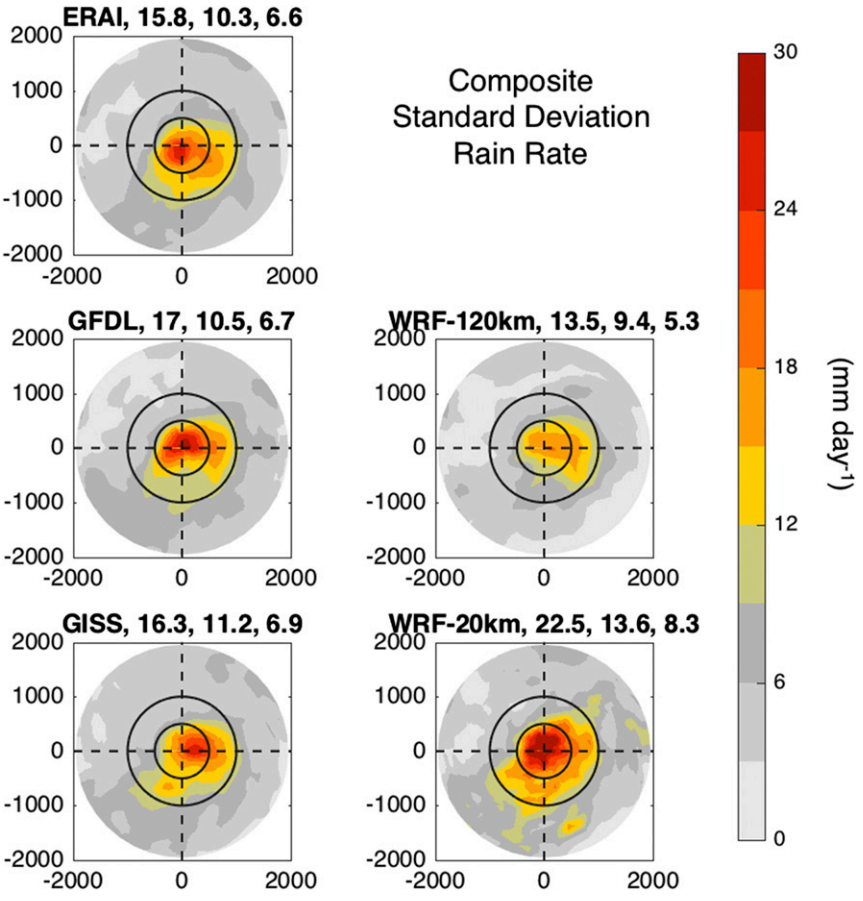

FIG. 3. As in Fig. 2, but for cyclone-centered composite standard deviation for precipitation.

model, which had finer spatial resolution than the reanalysis, produced more ETC precipitation than the reanalysis. As discussed in section 2, the differences between ERAI and the WRF-20km model are within the range of uncertainty of observations based on satellite data.

The spatial distribution of precipitation in the composite means is not representative of most individual cyclones, which tend to have thinner cold-frontal precipitation regions and more inhomogeneity in the precipitation rates near the fronts. This point is made clear in Fig. 3, which shows the standard deviation for the composited cyclones. The maximum in cyclone-to-cyclone variability is coincident with the maximum in the composite mean. As in Fig. 2, the GFDL model has more precipitation activity near the center and less along the cold front, indicating that this model concentrates its ETC precipitation in the warm sector. The larger standard deviation in the WRF-20km model is indicative of the model's well-resolved finescale frontal precipitation.

Composite means can sometimes hide differences because they involve averaging a large set of data. As such, we examine frequency distributions of precipitation rates for the data used to calculate the means (Fig. 4). For points within 1000 km of the cyclones' centers, the models all generate a similar distribution with a maximum at weak precipitation rates (i.e., 0–1 mm day^{-1}). ERAI and the WRF-20km model have larger relative frequencies of zero precipitation, and the WRF-20km model has the largest relative frequency of the strongest precipitation rates (Fig. 4a). If we consider points within 500 km of the cyclones' centers (Fig. 4b), the peak in the distribution shifts to larger values, between 8 and 16 mm day^{-1} for all models, except in WRF-20km. As discussed in section 2, the peak in weak precipitation in WRF-20km is not a result of regridding. WRF-20km again has the largest frequency of strong rates, suggesting a stronger potential impact of latent heating in conditions where latent heating would be expected to be large. If we compare the distributions for precipitation rates greater than 8 mm day^{-1}, the WRF-20km model significantly differs from the others, based on the method described in section 2. The propensity for WRF-20km to have stronger precipitation

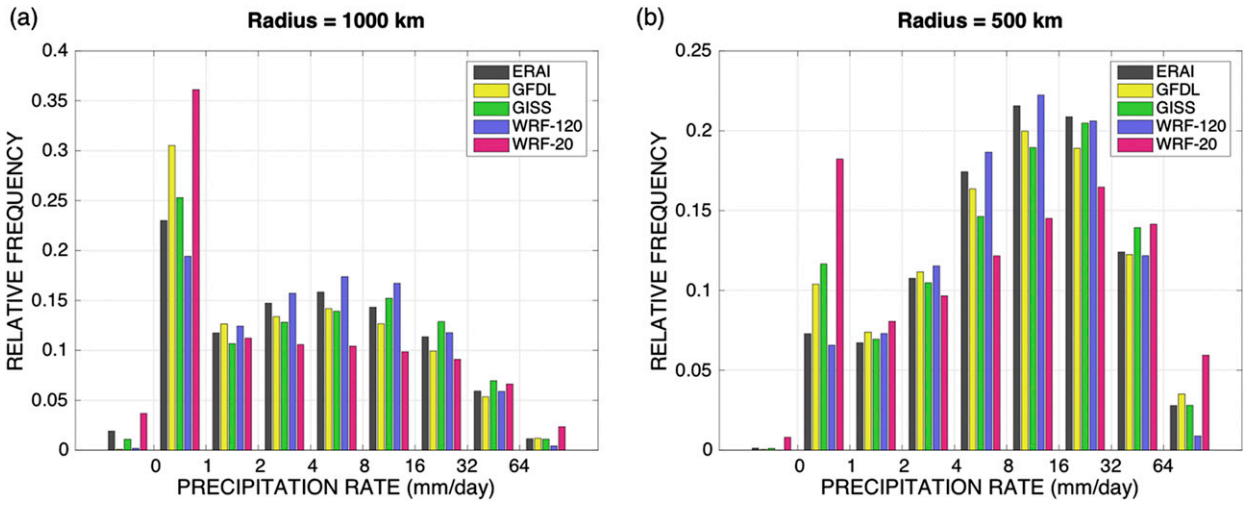

FIG. 4. Distribution of precipitation rates for all points in all cyclones that are in Fig. 2. All data within (a) 1000 and (b) 500 km of the cyclone centers. The bars to the left of 0 on the *x* axis indicate a zero precipitation rate; otherwise, the bars indicate precipitation rates in the range between the values shown on the *x* axis.

rates than the other models may be related to its finer resolution (e.g., Champion et al. 2011; Li et al. 2011).

The WRF-20km model has stronger cyclones dynamically and in terms of precipitation, consistent with the idea of latent heating interacting with cyclone circulation. However, a similar relationship is not found across the other datasets. ERAI has the stronger WSPD, but it has nearly equal precipitation rates to the GISS model. The GFDL model has stronger precipitation rates near the cyclone center but not stronger WSPD. The lack of a relationship between model-to-model differences in precipitation and dynamical cyclone strength could be the result of multiple factors, such as surface boundary conditions, dry baroclinic forcing, or biases in the modeled latent heating within the cyclone. Here we explore the latter factor, based on the hypothesis discussed in the introduction: it is possible that parameterized convection is interfering with the thermodynamic link between precipitation and cyclone strength. Therefore, the next analysis focuses on understanding the behavior of ETC precipitation from the convection schemes.

b. *ETC precipitation generated by convection parameterizations*

The reanalysis and models each use a different convection scheme (Table 1), and each saves convective precipitation as a standard output variable. We note that the convective precipitation output saved by models might only provide a minimum estimate of convective activity in the model. This is because 1) a convection scheme may activate and then pass moisture to the large-scale microphysics scheme where precipitation is generated and 2) a model may resolve some of the convection. Nonetheless, precipitation from the convective scheme serves as a conservative indicator of convective activity and highlights vertically unstable regions in cyclones. To improve the flow of the text, we refer to the precipitation from the convection scheme as the parameterized convective precipitation for the remainder of the results section.

For all models, parameterized convective precipitation is at most one-third the strength of the total composite mean precipitation (Fig. 5). However, model-to-model differences in the amplitude of precipitation from the convective scheme are large compared to total precipitation (e.g., 20% differences in the 500-km average). In terms of spatial distributions, all models have parameterized convective precipitation near the cold front, which is expected based on observations (e.g., Browning and Roberts 1996). However, for the GISS model, parameterized convective precipitation has a maximum coincident with the maximum for total precipitation in the warm sector. Precipitation rates in the convection composite are smallest in the WRF-20km model, perhaps because the model has a spatial resolution that can resolve some aspects of convection. Analysis of the distributions for convective precipitation (not shown) confirms the results shown in the composite mean analysis: (i) convective precipitation rates are smaller than the total precipitation rates, and (ii) ERAI and GISS, and to a lesser extent the GFDL model, more frequently have stronger parameterized convective precipitation, compared to the WRF RCMs.

To better understand if parameterized convective precipitation impacts ETC precipitation, we analyze its

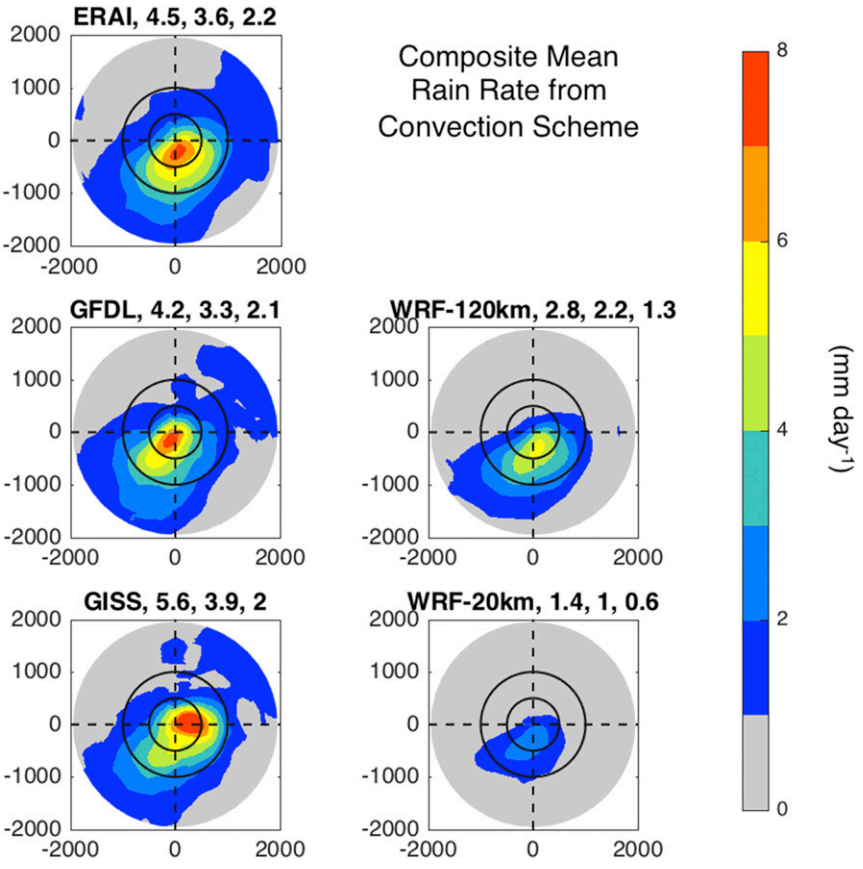

FIG. 5. As in Fig. 2, but for cyclone-centered composites of convective precipitation. Note the interval of this color bar is much smaller than in Fig. 2.

behavior. This work will include analysis of convective precipitation during cyclone life cycles; therefore, it considers all cyclones per track. We define a new metric for this analysis, convective fraction, as the cyclone-averaged precipitation from the convective scheme divided by cyclone-averaged total precipitation for each cyclone.

Figure 6 shows two-dimensional joint frequency distributions of cyclone-averaged precipitation and convective fraction. For ERAI, the most frequent precipitation rates have a convective fraction that ranges from 0 to 1 and most often is 0.4. At larger precipitation rates, the range and modal values of the convective fraction both decrease. The relationship between convective fraction and total precipitation in the GFDL and WRF-120km models is similar to ERAI. However, for WRF-120km the peak in frequency at weak precipitation rates occurs closer to zero. The WRF-20km model has an even smaller contribution from the convection scheme. The GISS model is unique because the convective fraction is most often near 0.4, and the range of convective fraction values is smaller than any of the other datasets. Thus, the GISS model regularly has 40% of its precipitation generated by the convection scheme, regardless of the overall precipitation rate. Despite this unique behavior, the composite and distribution for total ETC precipitation for the GISS model is similar to ERAI.

Next, we examine if convective fraction relates to an ETC's life cycle. We designate each cyclone (i.e., the 6-hourly snapshots) with a life cycle age that is relative to the time of peak WSPD for the track; that is, for each track, the cyclone with the maximum cyclone-averaged WSPD has age zero, and cyclones in the track that occur prior to peak WSPD have negative ages. Then, we divide each model's cyclone dataset in half, using the median value of convective fraction per dataset (see Fig. 6), and plot the distribution of cyclone life cycle age for the half of the cyclone with large convective fraction and the half with small convective fraction (Fig. 7). For all datasets, cyclones with larger convective fraction occur more frequently after the timing of peak WSPD (Fig. 7). These differences in the distributions are statistically significant. However, the separation between

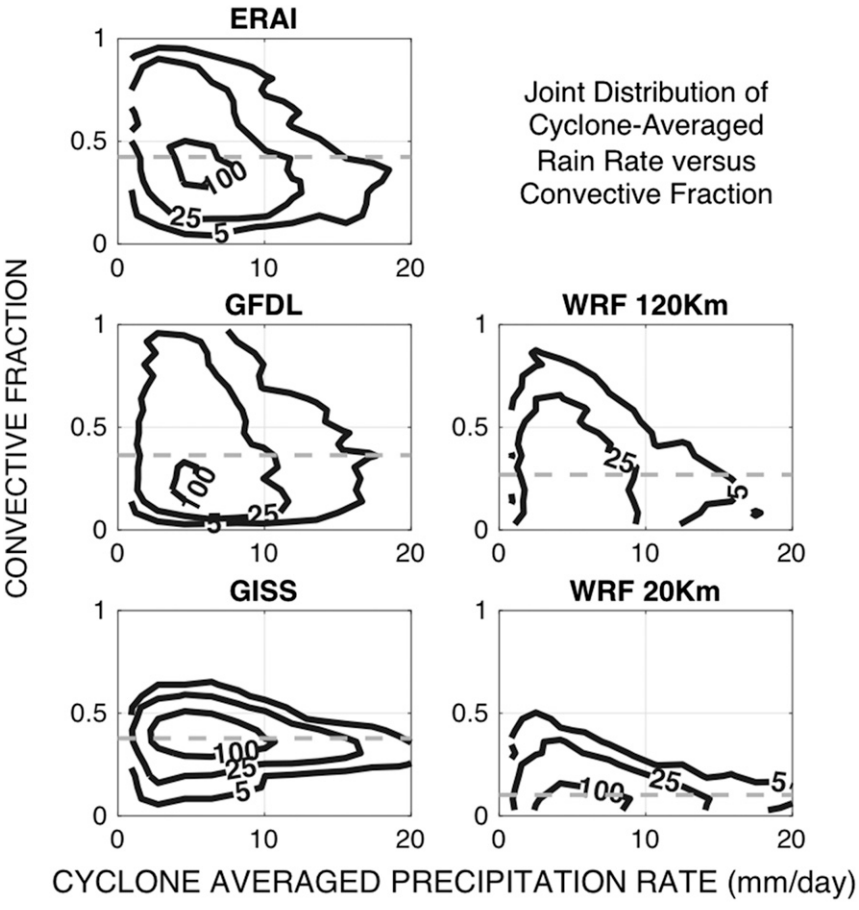

FIG. 6. Joint distribution of cyclone-averaged precipitation and convective fraction using all cyclones in all tracks. Units on contours are cyclone counts per 1.1 mm day^{-1} by 0.055 convective fraction bins. The gray dashed line cuts each set in two halves: top half with larger convective fraction and bottom half with smaller convective fraction.

the sets is more obvious for ERAI and the GFDL and WRF-120km models. This analysis shows that for a life cycle defined by WSPD the relative contribution of the convection scheme increases when the cyclone is decaying. If we define the life cycle using SLP, as in Pfahl and Sprenger (2016), we find a similar result. Also, for each model, the peak WSPD per track typically occurs coincident with or 6–12 h after peak precipitation for these datasets (not shown). Thus, Fig. 7 implies that larger convective fraction occurs more often when cyclone tracks are not generating peak precipitation. The peak in convective fraction during decay is associated with the evolution of the cyclone fronts, as we will discuss in the next section.

This section has revealed that the models have similarities and differences in the characteristics of parameterized convection in ETCs. The relative contribution of the convection scheme to total precipitation varies across the models; however, all of the models dictate the behavior of the parameterized convection based on the large-scale evolution of the tracks. With this in mind, we test the sensitivity of ETC precipitation to cyclone dynamics and thermodynamic conditions and check if the sensitivity is impacted by convective fraction strength.

c. *Sensitivity of precipitation to Q850 and WSPD*

Following FW2007, we use cyclone-averaged variables to subset the data and analyze how composite precipitation varies with cyclone moisture and surface wind speed. Following FW2007, we 1) calculate distributions of cyclone-averaged Q850 and WSPD, 2) divide each of the distributions into terciles, and 3) find the cyclones that fit into each of the nine resulting subcategories (Fig. 8). To link the analysis to convective fraction, we first divide the cyclones in half, based on strength of convective fraction, and then carry out the WSPD–Q850 subsetting for the strong and weak convective fraction cyclone sets separately per model. Thus,

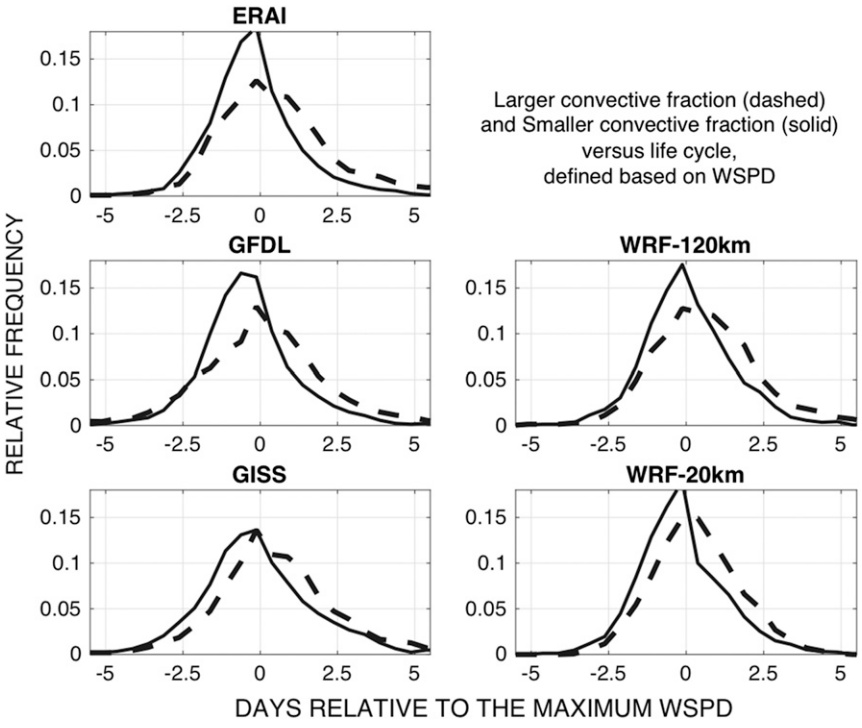

FIG. 7. Life cycle distributions relative to maximum WSPD for cyclones separated into two halves: those with larger convective fraction (dashed lines) and those with smaller convective fraction (solid lines).

the thresholds for the WSPD–Q850 analysis are defined separately for each convective fraction subset. Both WRF Model configurations differ from the other datasets by having few cyclones with large Q850 values (Fig. 8). This is mainly because WRF has fewer cyclones in the southern portion of the basin (Fig. 1b). The differences between the joint distributions of WSPD and Q850 for ERAI and the GFDL and GISS models are small, as are the differences between the large and small convective fraction subsets for each of the datasets.

The composite precipitation for WSPD–Q850 subsetting is displayed in a 3×3 panel: moving left to right, the columns have subsets with increasing WSPD, and moving from the bottom to top, the rows have subsets with increasing Q850. Figure 9 shows two of these 3×3 panels for the ERAI dataset, split in half based on convective fraction. The sensitivity to Q850 and WSPD is similar for both the smaller and larger convective fraction subsets: ETC precipitation increases with both Q850 and WSPD (Fig. 9). Fixing Q850 and increasing WSPD leads to an increase in the size of the comma structure of the composite. Fixing WSPD and increasing PWV leads to increases in the precipitation rates close to the cyclone center but has less of a change spatially. These results are consistent with FW2007.

Figure 9 (top) also shows that for ERAI, the cyclones with less convective fraction have 1) stronger precipitation rates and 2) a more defined comma shape. These results can both be related to the cyclone life cycle result (i.e., Fig. 7): convection occurs more frequently after peak precipitation when the cyclone track is reaching an occluded stage with a less well-defined comma structure. In this stage, there is the potential for more convectively generated precipitation (relative to the precipitation near the warm front generated by isentropic lift) near and behind the cold front because the spatial extent of cold advection over warm ocean water increases, and the cold front has caught up to the warm front, decreasing the size of the warm sector at the expense of the growing cold sector.

Figures 10a,f summarize the results shown in Fig. 8 for ERAI. For Figs. 10a,f, each horizontal bar is a cyclone-averaged precipitation value for one of the 3×3 panels in Fig. 9. Figure 10 shows results based on the 500-km cyclone average; however, the same result holds for the 1000- and 2000-km cyclone averages. By displaying the results of the WSPD–Q850 subsetting in this manner, it is possible to compare the relative changes in cyclone-averaged precipitation with respect to changes in Q850 (by focusing on a specific color in each panel) versus changes with respect to WSPD (by focusing on a subset

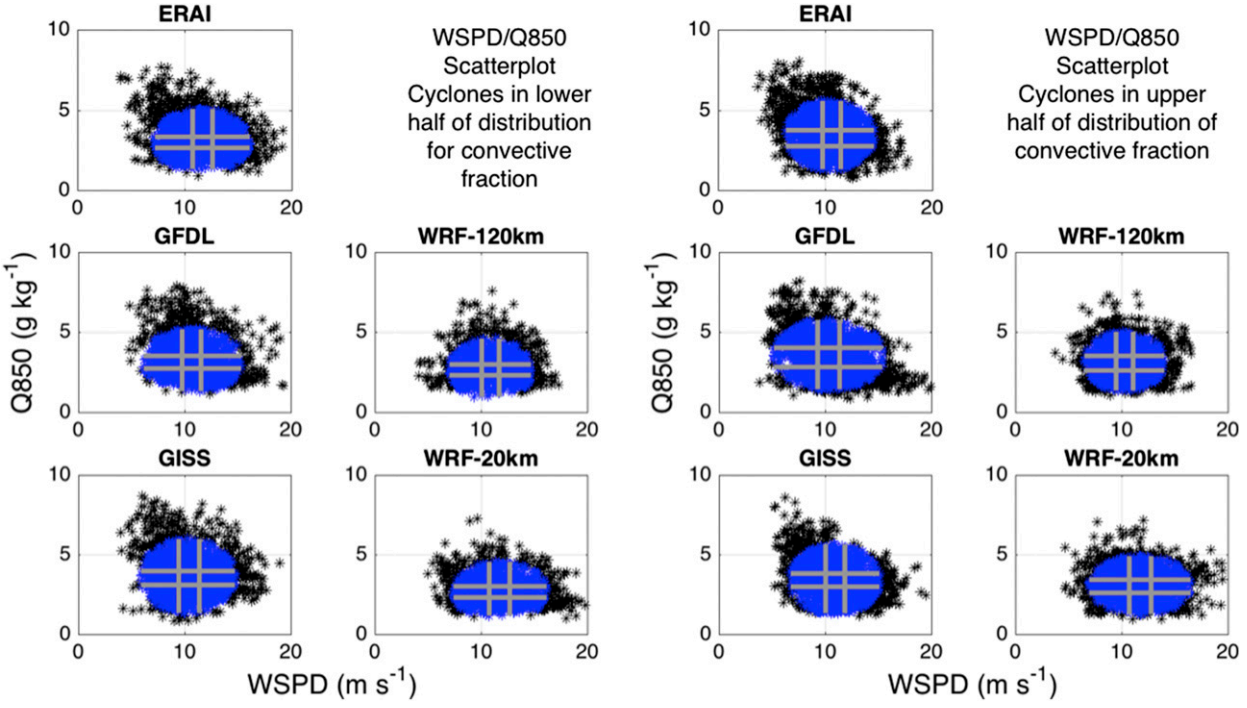

FIG. 8. Cyclone-averaged WSPD vs cyclone-averaged Q850 for (left) half of cyclones with smaller convective fraction and (right) half with larger convective fraction. Gray lines separate the data into equal-sized partitions for WSPD and Q850 separately. The resulting set of nine quadrants makes up the regions used for the partitioned analysis.

of three horizontal bars per panel). Figure 10 shows that these relative changes are similar both on a per-model basis and across multiple models.

Figure 10 shows the monotonic increase in precipitation with WSPD and Q850 that occurs in both convective fraction subsets. This result is important for two reasons: 1) it shows that ETC precipitation for these datasets covaries with moisture and dynamical strength in a manner similar to observations, and 2) this covariability is not influenced by parameterized convective precipitations. We also carried out this analysis for cyclone-averaged parameterized convective precipitation only. As with the total precipitation, composites of parameterized convective precipitation have monotonic increases in cyclone-averaged precipitation rates with increases in either WSPD or Q850, and this is true for both of the convective fraction subsets (not shown). Thus, the contribution of parameterized convective precipitation has the same sensitivity to cyclone WSDP and Q850 as the total cyclone precipitation.

Figure 10 also shows that for all models, the half of the set with weaker convective fraction has smaller precipitation rates. Thus, the relationships among cyclone life cycle, total precipitation, and parameterized convective precipitation that was discussed for ERAI applies to all of the models, given that all of the models and reanalysis have similar relationships between convective fraction and cyclone life cycle. This result provides a robust suggestion that convective fraction is dictated by the evolution of the cyclone life cycle rather than by the scheme dictating specific behavior in the cyclones or their life cycles.

4. Conclusions

The analysis herein compared extratropical cyclone precipitation for ERAI, two GCMs, and a WRF regional climate model integrated for resolutions of 120 and 20 km. Cyclone-centered composite analysis reveals that the GCMs generate a similar spatial distribution and amplitude of ETC precipitation as the reanalysis and the 20-km resolution WRF Model, with the latter generating slightly more ETC precipitation than the other models. By comparison, the 120-km resolution model had noticeably less ETC precipitation. Given that ERAI is a numerical weather model run in hindcast mode while assimilating observations, the fact that the GCMs generate similar composites implies the models represent ETC precipitation with reasonable skill.

This conclusion is made more interesting by the second main result of the analysis: the relative contribution of precipitation from the convection schemes differs

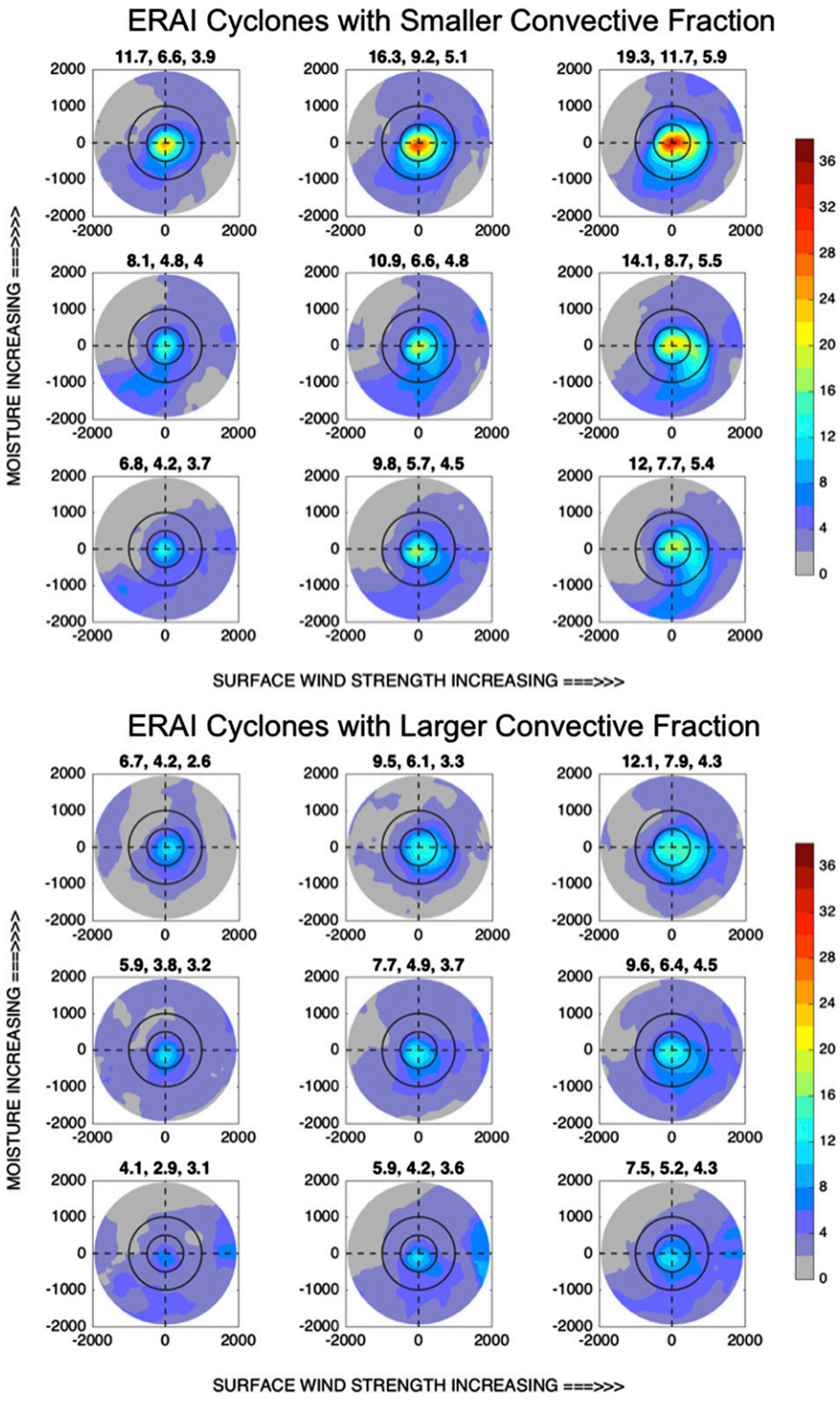

FIG. 9. Cyclone-centered precipitation composites for the ERAI subset, based on area-averaged WSPD and Q850 for (top) half of cyclones with smaller convective fraction and (bottom) half with larger convective fraction. Black circles indicate 500- (inner) and 1000-km (outer) radii. Values given above each panel are cyclone-averaged precipitation (mm day^{-1}) for 500, 1000, and 2000 km.

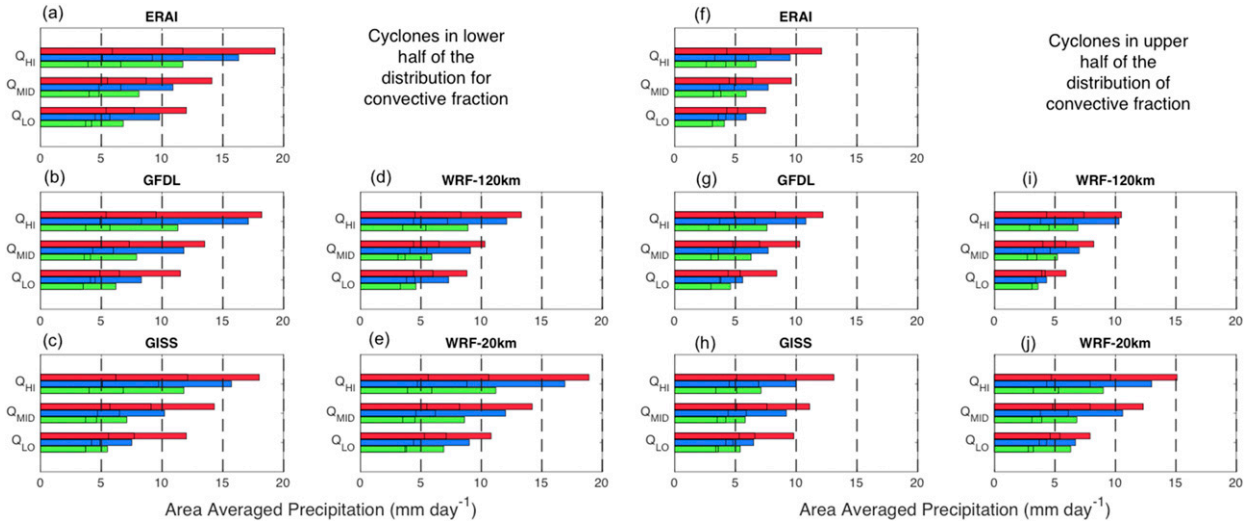

FIG. 10. Summary of the WSPD–Q850 subsetting analysis for (a)–(e) half of cyclones with smaller convective fraction and (f)–(j) half with larger convective fraction. The length of each bar is the 500-km cyclone-averaged precipitation rate for an individual precipitation composite from the subsetting analysis. QLO refers to the bottom row, QMID the middle row, and QHI the top row for Q850 in the 3×3 sets, and for each Q850 set, green corresponds to small WSPD, blue corresponds to medium WSPD, and magenta corresponds to large WSPD. In this figure, (a) and (f) correspond to the top and bottom 3×3 set of panels in Fig. 9, respectively.

between the reanalysis and GCMs by a larger fraction than the total precipitation differences. Thus, the GCMs and ERAI produce similar total composite precipitation accumulations, despite differences in the role of the convection scheme. Composite analysis reveals that in all models, the convection scheme generates precipitation in the region of the cyclone cold fronts. The WRF-20km model generates the least precipitation through its convection scheme, presumably because it partially resolves convection. ERAI, the GCMs, and the WRF-120km model also have differences in the relative contribution of the convection scheme to total precipitation, as seen in the composites and joint histograms of total precipitation and convective fraction. In particular, the GISS model stands out for having a convective fraction of 40%, even in cyclones with heavy precipitation. The unique behavior of the GISS model is also evident in the composite mean plot for the precipitation from the convection scheme, as it has the strongest rates in the warm sector near the cyclone center. Despite these differences, the overall performance of the GISS model in generating ETC precipitation matched ERAI and the GFDL model.

The nonnegligible contribution of the convection scheme to total precipitation in ERAI cannot yet be compared with observations. With the recently released NASA Global Precipitation Measurement (GPM; Skofronick-Jackson et al. 2017) radar–microwave radiometer combined product (Grecu et al. 2016), this may change in the near future. However, the work presented here focused on the relative similarities and differences in the precipitation generated by the convection schemes for ERAI, the GCMs, and WRF and examined if the differences affected the link between precipitation and cyclone surface wind strength.

For each model, we find that the contribution of precipitation from the convection scheme increases later in the cyclone life cycle, and typically this occurs after the time of peak precipitation per life cycle. As a result, cyclone composites comparing subsets with more and less convective fraction show that convective fraction is lower when more precipitation is present. However, we interpret the differences in total precipitation as a response of the ETCs to changes in the dynamical life cycle, rather than as a response to differences in convective precipitation. This conclusion is based on the next result we will discuss: the sensitivity analysis of precipitation relative to cyclone moisture and surface wind speed.

Based on a subsetting analysis, the cyclone-averaged ETC composite precipitation increases in response to increases in cyclone-averaged moisture or surface wind speed. This result holds for the reanalysis and all of the models, and it matches the results found in FW2007 for observations. Thus, the modeled ETC precipitation exhibits the correct response to changes in cyclone thermodynamic and dynamics conditions. This result holds true regardless of the strength of the contribution of the precipitation from the convection scheme, which gives another indication that the convection scheme does not have a significant impact on cyclone behavior.

We see the main results of the work as follows. The GCMs are capable of producing realistic ETC precipitation, on average. The GCMs and ERAI generate different amounts of precipitation with their convection schemes, and it does not affect the total precipitation. The ETC precipitation in the GCMs and WRF covaries with cyclone moisture and surface wind speed in a manner that matches reanalysis and observations. The precipitation generated by the convection scheme is noticeably influenced by cyclone life cycle and cyclone moisture and wind speed conditions, and a forcing in the opposite direction, from convection scheme to ETC behavior is not found. These results are based on composite analysis, and in individual cases the difference in the convection scheme may have a bigger impact. Furthermore, the heating from the convection scheme might impact storms in a manner not analyzed here (e.g., Hawcroft et al. 2017). However, in terms of the hypothesis described in the opening paragraph, the work here suggests that forcing on the ETC associated with changes in the warm conveyor belt due to the convection change is small.

Acknowledgments. Resources supporting this work were provided by the NASA High-End Computing (HEC) Program through the NASA Center for Climate Simulation (NCCS) at Goddard Space Flight Center. WRF and NCAR Command Language (NCL) were developed by the National Center for Atmospheric Research (NCAR). NCAR is sponsored by NSF. ERA-Interim data are provided by ECMWF online athttp://www.ecmwf.int/en/research/climate-reanalysis/era-interim. The authors especially thank Xiaobo Yang of ECMWF for providing the precipitation data. GFDL model data are provided by NOAA online at http://nomads.gfdl.noaa.gov:8080/DataPortal/cmip5.jsp. The research described in this manuscript was supported by the NOAA Climate Program Office's Modeling, Analysis, Predictions, and Projections program (Grant NA15OAR4310094) and the NASA PMM Science Team (Grant NNX16AD82G).

REFERENCES

Adler, R. F., and Coauthors, 2003: The Version-2 Global Precipitation Climatology Project (GPCP) monthly precipitation analysis (1979–present). *J. Hydrometeor.*, **4**, 1147–1167, https://doi.org/10.1175/1525-7541(2003)004<1147:TVGPCP>2.0.CO;2.

Bauer, M., and A. D. Del Genio, 2006: Composite analysis of winter cyclones in a GCM: Influence on climatological humidity. *J. Climate*, **19**, 1652–1672, https://doi.org/10.1175/JCLI3690.1.

——, G. Tselioudis, and W. B. Rossow, 2016: A new climatology for investigating storm influences in and on the extratropics. *J. Appl. Meteor. Climatol.*, **55**, 1287–1303, https://doi.org/10.1175/JAMC-D-15-0245.1.

Bengtsson, L., K. I. Hodges, and N. Keenlyside, 2009: Will extratropical storms intensify in a warmer climate? *J. Climate*, **22**, 2276–2301, https://doi.org/10.1175/2008JCLI2678.1.

Bleck, R., 2002: An oceanic general circulation model framed in hybrid isopycnic-Cartesian coordinates. *Ocean Modell.*, **4**, 55–88, https://doi.org/10.1016/S1463-5003(01)00012-9.

Booth, J. F., C. M. Naud, and A. D. Del Genio, 2013: Diagnosing warm frontal cloud formation in a GCM: A novel approach using conditional subsetting. *J. Climate*, **26**, 5827–5845, https://doi.org/10.1175/JCLI-D-12-00637.1.

——, E. Dunn-Sigouin, and S. Pfahl, 2017: The relationship between extratropical cyclone steering and blocking along the North American east coast. *Geophys. Res. Lett.*, **44**, 11 976–11 984, https://doi.org/10.1002/2017GL075941.

Boutle, I. A., S. E. Belcher, and R. S. Plant, 2011: Moisture transport in midlatitude cyclones. *Quart. J. Roy. Meteor. Soc.*, **137**, 360–373, https://doi.org/10.1002/qj.783.

Browning, K. A., and N. M. Roberts, 1996: Variation of frontal and precipitation structure along a cold front. *Quart. J. Roy. Meteor. Soc.*, **122**, 1845–1872, https://doi.org/10.1002/qj.49712253606.

Carlson, T. N., 1998: *Mid-Latitude Weather Systems*. Amer. Meteor. Soc., 507 pp.

Catto, J. L., L. C. Shaffrey, and K. I. Hodges, 2010: Can climate models capture the structure of extratropical cyclones? *J. Climate*, **23**, 1621–1635, https://doi.org/10.1175/2009JCLI3318.1.

Champion, A. J., K. I. Hodges, L. O. Bengtsson, N. S. Keenlyside, and M. Esch, 2011: Impact of increasing resolution and a warmer climate on extreme weather from Northern Hemisphere extratropical cyclones. *Tellus*, **63A**, 893–906, https://doi.org/10.1111/j.1600-0870.2011.00538.x.

Chen, C. T., and T. Knutson, 2008: On the verification and comparison of extreme rainfall indices from climate models. *J Climate*, **21**, 1605–1621, https://doi.org/10.1175/2007JCLI1494.1.

Dee, D. P., and Coauthors, 2011: The ERA-Interim reanalysis: Configuration and performance of the data assimilation system. *Quart. J. Roy. Meteor. Soc.*, **137**, 553–597, https://doi.org/10.1002/qj.828.

Donner, L. J., 1993: A cumulus parameterization including mass fluxes, vertical momentum dynamics, and mesoscale effects. *J. Atmos. Sci.*, **50**, 889–906, https://doi.org/10.1175/1520-0469(1993)050<0889:ACPIMF>2.0.CO;2.

——, and Coauthors, 2011: The dynamical core, physical parameterizations, and basic simulation characteristics of the atmospheric component AM3 of the GFDL global coupled model CM3. *J. Climate*, **24**, 3484–3519, https://doi.org/10.1175/2011JCLI3955.1.

Emanuel, K. A., M. Fantini, and A. J. Thorpe, 1987: Baroclinic instability in an environment of small stability to slantwise moist convection. Part I: Two-dimensional models. *J. Atmos. Sci.*, **44**, 1559–1573, https://doi.org/10.1175/1520-0469(1987)044<1559:BIIAEO>2.0.CO;2.

Field, P. R., and R. Wood, 2007: Precipitation and cloud structure in midlatitude cyclones. *J. Climate*, **20**, 233–254, https://doi.org/10.1175/JCLI3998.1.

——, A. Gettelman, R. B. Neale, R. Wood, P. J. Rasch, and H. Morrison, 2008: Midlatitude cyclone compositing to constrain climate model behavior using satellite observations. *J. Climate*, **21**, 5887–5903, https://doi.org/10.1175/2008JCLI2235.1.

Grecu, M., W. S. Olson, S. J. Munchak, S. Ringerud, L. Liao, Z. Haddad, B. L. Kelley, and S. F. McLaughlin, 2016: The GPM combined algorithm. *J. Atmos. Oceanic Technol.*, **33**, 2225–2245, https://doi.org/10.1175/JTECH-D-16-0019.1.

Hawcroft, M. K., L. Shaffrey, K. Hodges, and H. Dacre, 2012: How much Northern Hemisphere precipitation is associated with extratropical cyclones? *Geophys. Res. Lett.*, **39**, L24809, https://doi.org/10.1029/2012GL053866.

——, L. C. Shaffrey, K. I. Hodges, and H. F. Dacre, 2016: Can climate models represent the precipitation associated with extratropical cyclones? *Climate Dyn.*, **47**, 679–695, https://doi.org/10.1007/s00382-015-2863-z.

——, H. Dacre, R. Forbes, K. Hodges, L. Shaffrey, and T. Stein, 2017: Using satellite and reanalysis data to evaluate the representation of latent heating in extratropical cyclones in a climate model. *Climate Dyn.*, **48**, 2255–2278, https://doi.org/10.1007/s00382-016-3204-6.

Hodges, K. I., R. W. Lee, and L. Bengtsson, 2011: A comparison of extratropical cyclones in recent reanalyses ERA-Interim, NASA MERRA, NCEP CFSR, and JRA-25. *J. Climate*, **24**, 4888–4906, https://doi.org/10.1175/2011JCLI4097.1.

Kim, D., A. D. Del Genio, and M.-S. Yao, 2011: Moist convection scheme in Model E2. NOAA Tech. Note, 9 pp., http://www.giss.nasa.gov/tools/modelE/docs/kim_moistconvection.pdf.

Leckebusch, G. C., D. Renggli, and U. Ulbrich, 2008: Development and application of an objective storm severity measure for the Northeast Atlantic region. *Meteor. Z.*, **17**, 575–587, https://doi.org/10.1127/0941-2948/2008/0323.

Li, F., W. D. Collins, M. F. Wehner, D. L. Williamson, and J. G. Olson, 2011: Response of precipitation extremes to idealized global warming in an aqua-planet climate model: Towards a robust projection across different horizontal resolutions. *Tellus*, **63A**, 876–883, https://doi.org/10.1111/j.1600-0870.2011.00543.x.

Martin, J. E., 2006: *Mid-Latitude Atmospheric Dynamics: A First Course.* Wiley, 336 pp.

Michaelis, A. C., J. Willison, G. M. Lackmann, and W. A. Robinson, 2017: Changes in winter North Atlantic extratropical cyclones in high-resolution regional pseudo–global warming simulations. *J. Climate*, **30**, 6905–6925, https://doi.org/10.1175/JCLI-D-16-0697.1.

NCEP/NWS/NOAA/U.S. Department of Commerce, 2000: NCEP FNL Operational Model Global Tropospheric Analyses, continuing from July 1999. Research Data Archive at the National Center for Atmospheric Research, Computational and Information Systems Laboratory, accessed 15 March 2017, https://doi.org/10.5065/D6M043C6.

Neu, U., and Coauthors, 2013: IMILAST: A community effort to intercompare extratropical cyclone detection and tracking algorithms. *Bull. Amer. Meteor. Soc.*, **94**, 529–547, https://doi.org/10.1175/BAMS-D-11-00154.1.

Pfahl, S., and M. Sprenger, 2016: On the relationship between extratropical cyclone precipitation and intensity. *Geophys. Res. Lett.*, **43**, 1752–1758, https://doi.org/10.1002/2016GL068018.

Pithan, F., T. G. Shepherd, G. Zappa, and I. Sandu, 2016: Climate model biases in jet streams, blocking and storm tracks resulting from missing orographic drag. *Geophys. Res. Lett.*, **43**, 7231–7240, https://doi.org/10.1002/2016GL069551.

Rudeva, I., and S. K. Gulev, 2011: Composite analysis of North Atlantic extratropical cyclones in NCEP–NCAR reanalysis data. *Mon. Wea. Rev.*, **139**, 1419–1446, https://doi.org/10.1175/2010MWR3294.1.

Schmidt, G. A., and Coauthors, 2014: Configuration and assessment of the GISS ModelE2 contributions to the CMIP5 archive. *J. Adv. Model. Earth Syst.*, **6**, 141–184, https://doi.org/10.1002/2013MS000265.

Shimkus, C., M. Ting, J. F. Booth, S. B. Adamo, M. Madajewicz, Y. Kushnir, and H. E. Rieder, 2017: Winter storm intensity, hazards, and property losses in the New York tristate area. *Ann. N. Y. Acad. Sci.*, **1400**, 65–80, https://doi.org/10.1111/nyas.13396.

Skamarock, W. C., and Coauthors, 2008: A description of the Advanced Research WRF version 3. NCAR Tech. Note NCAR/TN-475+STR, 113 pp., https://doi.org/10.5065/D68S4MVH.

Skofronick-Jackson, G., and Coauthors, 2017: The Global Precipitation Measurement (GPM) mission for science and society. *Bull. Amer. Meteor. Soc.*, **98**, 1679–1695, https://doi.org/10.1175/BAMS-D-15-00306.1.

Stoelinga, M. T., 1996: A potential vorticity-based study on the role of diabatic heating and friction in a numerically simulated baroclinic cyclone. *Mon. Wea. Rev.*, **124**, 849–874, https://doi.org/10.1175/1520-0493(1996)124<0849:APVBSO>2.0.CO;2.

Tiedtke, M., 1989: A comprehensive mass flux scheme for cumulus parameterization in large-scale models. *Mon. Wea. Rev.*, **117**, 1779–1800, https://doi.org/10.1175/1520-0493(1989)117<1779:ACMFSF>2.0.CO;2.

Walz, M. A., T. Kruschke, H. W. Rust, U. Ulbrich, and G. C. Leckebusch, 2017: Quantifying the extremity of windstorms for regions featuring infrequent events. *Atmos. Sci. Lett.*, **18**, 315–322, https://doi.org/10.1002/asl.758.

Willison, J., W. A. Robinson, and G. M. Lackmann, 2015: North Atlantic storm-track sensitivity to warming increases with model resolution. *J. Climate*, **28**, 4513–4524, https://doi.org/10.1175/JCLI-D-14-00715.1.

Yao, M. S., and A. D. Del Genio, 1989: Effects of cumulus entrainment and multiple cloud types on a January global climate model simulation. *J. Climate*, **2**, 850–863, https://doi.org/10.1175/1520-0442(1989)002%3C0850:EOCEAM%3E2.0.CO;2.

Yettella, V., and J. E. Kay, 2017: How will precipitation change in extratropical cyclones as the planet warms? Insights from a large initial condition climate model ensemble. *Climate Dyn.*, **49**, 1765–1781, https://doi.org/10.1007/s00382-016-3410-2.

Zappa, G., L. C. Shaffrey, and K. I. Hodges, 2013: The ability of CMIP5 models to simulate North Atlantic extratropical cyclones. *J. Climate*, **26**, 5379–5396, https://doi.org/10.1175/JCLI-D-12-00501.1.

Zhang, G. J., and N. A. McFarlane, 1995: Sensitivity of climate simulations to the parameterization of cumulus convection in the Canadian Climate Centre general circulation model. *Atmos.–Ocean*, **33**, 407–446, https://doi.org/10.1080/07055900.1995.9649539.